

Article

Theoretical Analysis for Improving the Efficiency of HT-PEMFC through Unreacted Hydrogen Circulation

Sanghyoun Park  and Sangyong Lee * 

Mechanical Robotics and Energy Department, Dongguk University, Seoul 04620, Republic of Korea; psh6851@naver.com

* Correspondence: sangyonglee@dongguk.edu

Abstract: To increase the efficiency of a fuel processor and HT-PEMFC (high temperature-proton exchange membrane fuel cell) combined system, it is essential to improve the efficiency of the fuel processor. In this research, the fuel processor was simulated by the Aspen Hysys[®] simulator, and the effect of the various operating conditions on the total efficiency was investigated. The thermal efficiency of the fuel processor increased as the temperature and S/C (steam-to-carbon) ratio increased, and the efficiency was higher at an S/C ratio of 3 than at an S/C of 4 with a reformer temperature of 700 °C and higher. Under the selected operating conditions of the fuel processor, the recycling of unreacted hydrogen from the anode off-gas (AOG) of the HT-PEMFC improved the overall efficiency of the combined fuel processor and HT-PEMFC by a factor of 1.28. The operating conditions where the AOG supplied more heat than was required for fuel processor operation were excluded. The high-efficiency operating conditions of the fuel cell system were proposed with the target of 5 kW of output as the capacity of the household HT-PEMFC.

Keywords: fuel processor; steam reformer; residential HT-PEMFC; fuel cell; water–gas shift reactor



Citation: Park, S.; Lee, S. Theoretical Analysis for Improving the Efficiency of HT-PEMFC through Unreacted Hydrogen Circulation. *Appl. Sci.* **2023**, *13*, 9292. <https://doi.org/10.3390/app13169292>

Academic Editor: Aliaksandr Shaula

Received: 17 July 2023

Revised: 11 August 2023

Accepted: 14 August 2023

Published: 16 August 2023



Copyright: © 2023 by the authors. Licensee MDPI, Basel, Switzerland. This article is an open access article distributed under the terms and conditions of the Creative Commons Attribution (CC BY) license (<https://creativecommons.org/licenses/by/4.0/>).

1. Introduction

Distributed power generation is actively researched as a response to the instability of power supplies, such as a large-scale blackout, due to disaster. Distributed power generation directly produces and supplies power at demand, and stationary fuel cells are representative of distributed power generation [1,2]. Stationary fuel cells for buildings have the advantages of using a relatively small installation space for producing the same amount of energy compared to other renewable energies and using the existing city gas infrastructure [3,4]. Therefore, the demand for stationary fuel cell systems for buildings is increasing worldwide. Also, the electricity output, durability, system size, operation, installation, and operation costs of fuel cell systems are becoming competitive [5,6]. In particular, the efficiency of a fuel processor and fuel cell combined system is mainly affected by the fuel processor efficiency [7,8]. The flow rate of methane used for the reactants and burner fuel affects the reaction temperature in the steam reformer, resulting in a change in conversion and affecting the overall efficiency of the combined system [9]. In general, the hydrogen production rate increases as the temperature of the reactor increases, but the overall thermal efficiency may decrease due to the excessive input of burner fuel [10]. Therefore, the fuel processor needs to be operated at optimal temperature conditions and operate within the temperature range shown in Figure 1.

The fuel processor is composed of a steam reformer, a water–gas shift reactor, a burner, a desulfurizer, and heat exchangers [11]. In a steam reformer, natural gas and steam react on nickel catalysts at 500 °C to 800 °C to produce hydrogen and carbon monoxide [12]. Since the reforming reaction is endothermic, the reactor must be designed to supply a sufficient amount of heat to keep the reaction temperature constant [13,14]. For this reason, a burner is installed close to where the steam reforming reaction takes place to provide sufficient thermal energy.

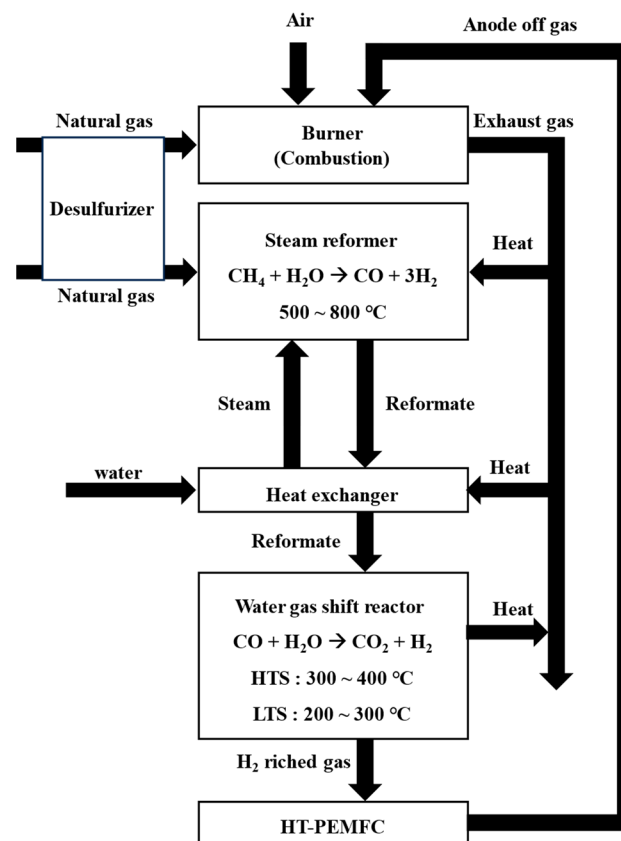


Figure 1. Schematic diagram of the fuel processor.

The heat from the exhaust gas, the reformed gas, and released from the steam reformer is recovered to heat the reactants, in particular, water [15]. Increasing the efficiency of fuel processors requires thermal energy optimization for the heat transfer between the exhaust gas, reformat, and reactants.

The WGS (water–gas shift reactor) is classified into either an HTS (high-temperature shift reactor) or LTS (low-temperature shift reactor) depending on the operating temperature (shown in Figure 1). The WGS reactor shifts CO to CO₂ to prevent CO poisoning of the fuel cell. A water–gas shift reaction is an exothermic reaction so it is necessary to remove the reaction heat [16]. The LT-PEMFC (low temperature-proton exchange membrane fuel cell) requires the CO concentration to be less than 10 ppm [17,18], whereas the HT-PEMFC (high temperature-proton exchange membrane fuel cell) has sufficient durability, even when the CO concentration is less than 1% [17]. As such, HT-PEMFCs may have greater tolerance to some impurities, such as carbon monoxide (CO) and sulfur compounds, than LT-PEMFCs. This is economically useful as it eliminates the purification process, similar to a preferential reactor. In addition, since the HT-PEMFC operates at a higher temperature (120 to 180 °C) than the LT-PEM (60 to 80 °C) fuel cell, the utilization of waste heat such as tri-generation is increased and the overall efficiency is increased [17–20]. However, despite these benefits, combined systems of fuel processors and HT-PEMFCs can release more CO pollutants into the atmosphere. Therefore, CO reduction as well as heat recovery should be achieved at the burner by recycling the anode off-gas to the burner.

One of the ways to increase the total efficiency of the fuel processor and fuel cell combined system is to recirculate the unreacted hydrogen discharged from the anode of the fuel cell to the burner as a fuel [21–26]. The attempts to circulate unreacted hydrogen to a burner have mainly been performed on low-temperature PEMFC systems. For HT-PEMFC, there has been a lack of analysis of the system using unreacted hydrogen.

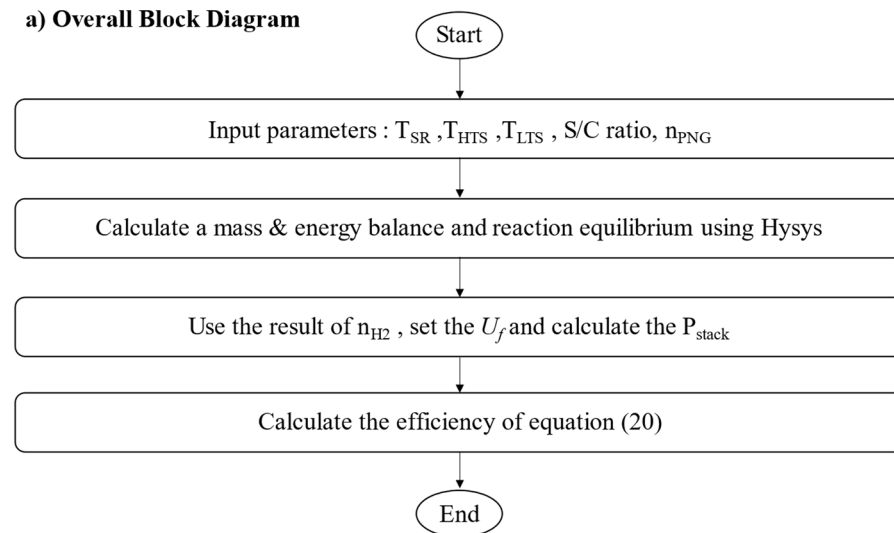
In this study, conditions such as the operating temperature, S/C ratio, reactant flow rate, and burner fuel flow rate of each reactor were investigated to efficiently operate

the combined system of the fuel processing system and HT-PEMFC stack. A theoretical model based on thermodynamic analysis was applied and the overall efficiency of the combined process was investigated at various operating temperatures using the Aspen Hysys[®] simulator.

2. Modeling

Simulations were performed for a combined system of a fuel processor and HT-PEMFC with a recycle stream of anode off-gas to a burner installed in the SR (steam reformer). Figure 2 shows the simulation process for the combined system of a fuel processor and HT-PEMFC.

a) Overall Block Diagram



b) Block Diagram for P_{stack}

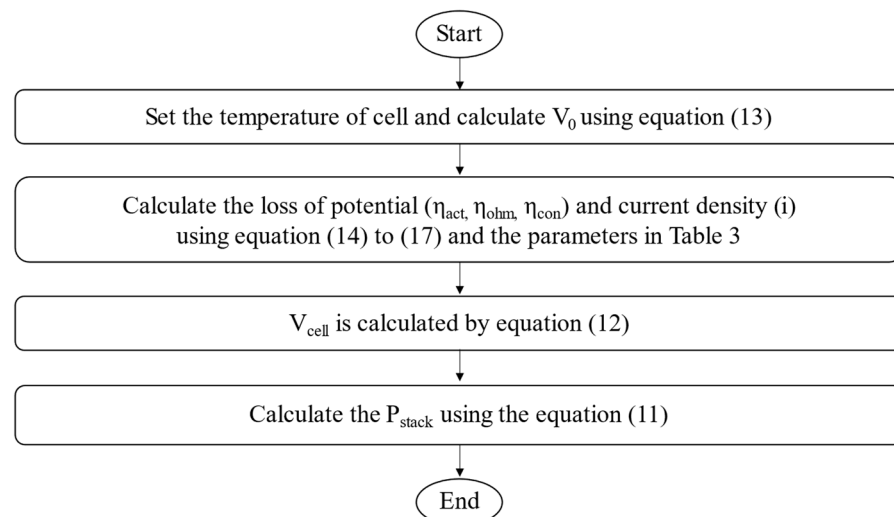


Figure 2. Simulation block diagram, (a) overall block diagram for the fuel processor and HT-PEMFC and (b) block diagram for the P_{stack} calculation.

2.1. Fuel Processor Description

Simulations were performed for a combined system of a fuel processor and HT-PEMFC with a recycle stream of anode off-gas to a burner installed in the SR (steam reformer). The fuel processing system consists of a steam reformer, two water–gas shift reactors (a high-temperature shift reactor and a low-temperature shift reactor), and heat exchangers. Figure 3 shows the process flow diagram by Aspen Hysys[®]. PNG (process natural gas)

is introduced to the reformer and reacted with steam to form hydrogen. Q_{H1} is the heat required to raise the PNG to the reaction temperature of the steam reformer. Q_{H2} is the heat required to turn water into steam up to the reaction temperature of the reformer. The product gas from the steam reformer is cooled down by a heat exchanger (cooler 1 in Figure 3) to the high-temperature water–gas shift reactor (HTS) operating temperature and then introduced to the HTS. CO is then converted into CO_2 with steam at the HTS and the concentration of CO in the HTS product gas is lowered to less than 3%. To reduce the CO concentration lower than 1%, the HTS product gas is cooled again and introduced to the low-temperature water–gas shift reactor [27]. The heat released in the process is named Q_{c1} , Q_{c2} , and Q_{c3} . Q_{SR} is the energy required for the reaction at the steam reformer. Q_{HTS} is the heat of the reaction at the high-temperature water–gas shift reactor and Q_{LTS} is the heat of the reaction at the low-temperature water–gas shift reactor.

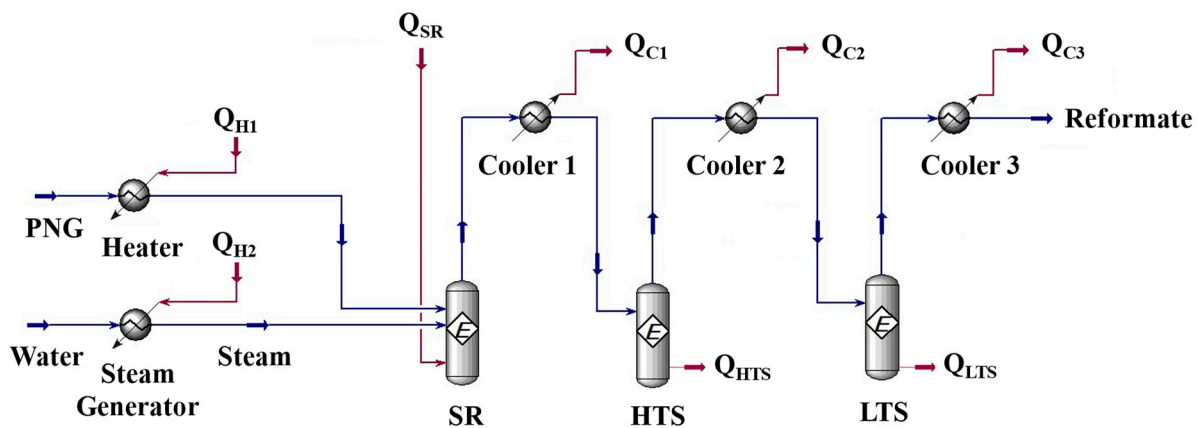
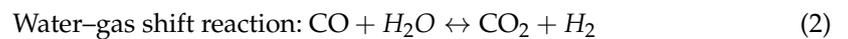
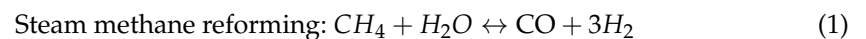


Figure 3. Aspen hysys® flowsheet of the fuel processor.

In the steam reformer, two main reactions are considered [28–30]: the steam reforming reaction (Equation (1)) and the WGS reaction (Equation (2)). It is assumed that the reaction proceeds to equilibrium conditions in each reactor, and the equilibrium reactor is used for the simulation with the equilibrium constants (K_{SR} and K_{WGS}) calculated in Equations (3) and (4).



$$K_{SR} = \frac{p_{CO}p_{H_2}^3}{p_{CH_4}p_{H_2O}} atm^{-2} = \frac{1}{\exp(Z(Z(Z(0.2513Z - 0.3665) - 0.58101) + 27.1337) - 3.2770)} \quad (3)$$

$$K_{WGS} = \frac{p_{H_2}p_{CO_2}}{p_{H_2O}p_{CO}} atm^{-2} = \exp(Z(Z(0.63508 - 0.29353Z) + 4.1778) + 0.31688) \quad (4)$$

$$Z = \left(\frac{1000}{T} \right) - 1 \quad (5)$$

Equations (3) and (4) are empirical equations presented by Twigg [31], and the equilibrium constants (K_{SR} and K_{WGS}) are expressed as a function of temperature (Z and T) instead of each partial pressure. The WGS reactor applied K_{WGS} within the temperature range of the reactor. The equilibrium constants calculated for each reaction are summarized in Table 1.

Table 1. The equilibrium constants for reactor temperatures.

T_{SR} (°C)	Equilibrium Constant	
	Steam Reforming (K_{SR})	Water–Gas Shift (K_{WGS})
100	0	2289
200	0	210.8
300	0	38.83
400	0.0001	11.72
500	0.0098	4.904
600	0.5212	2.551
700	12.54	1.541
800	168.87	1.036

To calculate the thermal energy and heat of the reaction in each component, energy balances are applied. As shown in Figure 4, the fuel processor consists of two independent parts. One is the reaction part and the other is the thermal energy supply part. The thermal energy required is calculated as the enthalpy difference between the inlet stream and the outlet stream (Equations (6) and (7)), which can be supplied by the methane burner via combustion. Since the entire system must operate at a steady state, the total reactive energy required (Q_{RE}) is equal to the amount of energy supplied by the burner through combustion (Q_{CE}).

$$Q_{CE} = \sum_{\text{Thermal energy supply part}} \dot{m}_i h_i = \dot{m}_{fuel} \Delta h_{fuel} + \dot{m}_{Air} \Delta h_{Air} - \dot{m}_{Exhaust\ gas} \Delta h_{Exhaust\ gas} \quad (6)$$

$$Q_{RE} = \sum_{\text{Reaction part}} \dot{m}_i h_i = \dot{m}_{PNG} \Delta h_{PNG} + \dot{m}_{Water} \Delta h_{water} - \dot{m}_{Reformate} \Delta h_{Reformate} \quad (7)$$

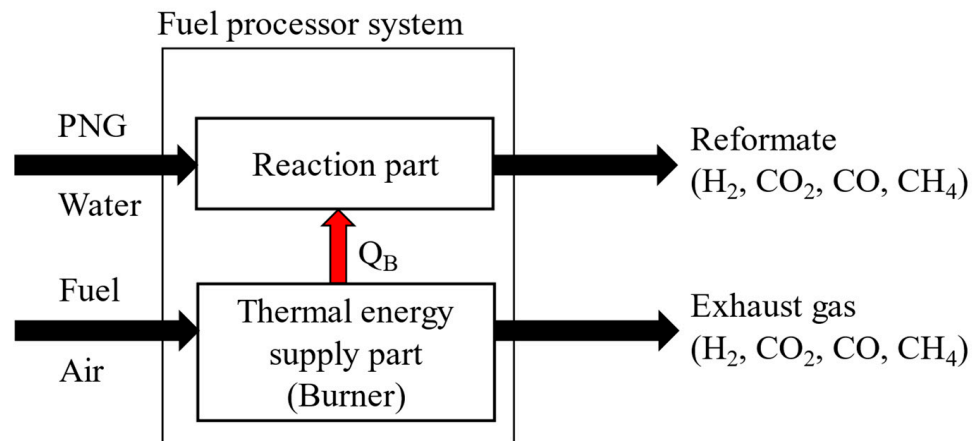


Figure 4. Schematic diagram of the energy balance of the fuel processor system.

The required energy of the reaction section can be calculated by summing the heat of the reaction and the heat energy for heating the reactants, or for cooling the products as shown in Equation (8). In Equation (8), each energy is calculated by the enthalpy difference between the inlet stream and outlet stream. The enthalpy of each stream is a function of the temperature, flow rate, and degree of reaction.

$$Q_{RE} = -Q_{H1} - Q_{H2} - Q_{SR} + Q_{C1} + Q_{C2} + Q_{C3} + Q_{HTS} + Q_{LTS} \quad (8)$$

Figure 5 shows the above explanation intuitively.

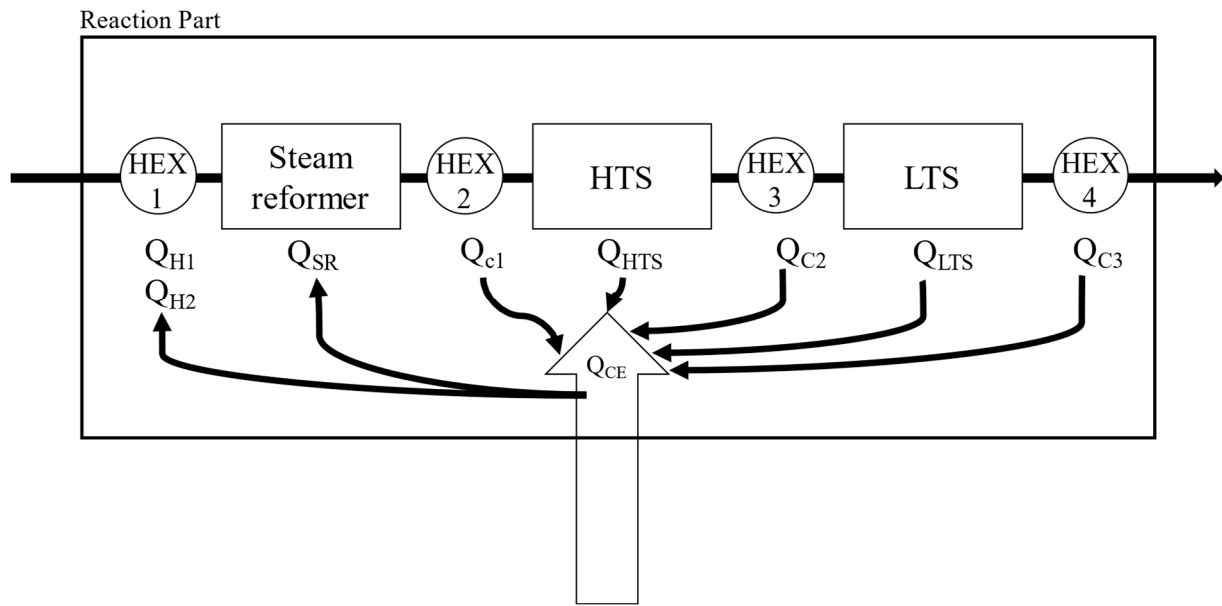


Figure 5. Detailed thermal energy flow of the reaction part.

The thermal efficiency of the fuel processor system (η_{FP}) is defined as Equation (9) [32–34].

$$\eta_{FP} = \frac{n_{H_2} LHV_{H_2}}{(n_{BNG} + n_{PNG}) * LHV_{NG} + n_{AOG H_2} LHV_{AOG H_2} + n_{AOG CH_4} LHV_{CH_4}} \quad (9)$$

The thermal efficiency of the fuel processor is calculated by dividing the energy of the produced hydrogen by the total energy supplied to the process (PNG, natural gas to the burner, AOG). Energy is expressed as the product of the moles and lower heating value (LHV). The n_{BNG} is the number of moles of natural gas introduced to the burner, and the n_{PNG} is the number of moles of natural gas introduced to the reaction part. The hydrogen and methane moles in AOG are denoted by $n_{AOG H_2}$ and $n_{AOG CH_4}$.

The product gas containing the produced hydrogen is cooled in the cooler Q_{C3} system to remove the moisture in the product gas and is then supplied to the PEMFC. Hydrogen is supplied to the anode side and oxygen from the air is supplied to the cathode side of the PEMFC. Using an electrochemical reaction, electrical energy is produced. To calculate the amount of electrical energy produced by the PEMFC, fuel utilization efficiency and the irreversibility of the PEMFC should be considered. The detailed simulation condition for the fuel processing system is summarized in Table 2.

Table 2. Simulation conditions for the fuel processing system.

Variables	Condition
Temperature of steam reformer (T_{SR})	500~900 °C
Temperature of HTS (T_{HTS})	300~400 °C
Temperature of LTS (T_{LTS})	200~300 °C
Steam-to-carbon ratio (S/C)	1~5
The molar flow rate of natural gas supplied to steam reformer (\dot{n}_{PNG})	0.7~1.2 mol/min

The S/C ratio is defined as in Equation (10) and is a value obtained by dividing the moles of steam introduced by the moles of carbon.

$$S/C \text{ ratio} = \frac{\text{Steam moles}}{\text{Carbon moles}} \quad (10)$$

2.2. PEMFC Description

Since the flow rate of unreacted hydrogen in the AOG is inversely proportional to the fuel utilization efficiency of the PEMFC, the proper prediction of fuel utilization efficiency is important to calculate the hydrogen consumption rate in the PEMFC. Power by the PEMFC stack (P_{stack}) can be calculated as the product of the number of the unit cell (n_{cell}), unit cell voltage (V_{cell}), unit cell current (i), and MEA area (A_{MEA}), as shown in Equation (11).

$$P_{stack} = n_{cell} V_{cell} \cdot i \cdot A_{MEA} \tag{11}$$

The unit cell voltage in Equation (11) can be calculated from Equation (12) and considering the thermodynamic equilibrium potential (V_o) and the irreversibility of the PEMFC, such as the activation loss (η_{act}), ohmic loss (η_{ohm}), and concentration loss (η_{con}) [35].

$$V_{cell} = V_o - \eta_{act} - \eta_{ohm} - \eta_{con} \tag{12}$$

The thermodynamic equilibrium potential, activation loss, ohmic loss, and concentration loss are calculated by Equations (13)–(17). Equation (13) can calculate the thermodynamic equilibrium potential in the HT-PEMFC. Equation (13) is a function of cell temperature (T_{cell}) and 1.1549 V was calculated using a cell temperature of 150 °C [36].

$$V_o = 1.1669 - 0.00024(T_{cell} - 373.15) \tag{13}$$

Activation loss can be calculated by the Butler–Volmer equation that expresses electrochemical kinetics [35]. Since the hydrogen oxidation reaction and oxygen reduction reaction occur in the anode and cathode in fuel cells, the Butler–Volmer equation uses the two half-reactions of Equations (14) and (15) to calculate the activation loss [35–39].

$$\eta_{act,a} = \frac{i}{i_{0,a}^{ref}} \frac{RT_{cell}}{(\alpha_a + \alpha_c F)} \left(\frac{C_{H_2,ref}}{C_{H_2}} \right)^{0.5} \tag{14}$$

$$|\eta_{act,c}| = \frac{RT_{cell}}{\alpha_c F} \ln \left[\left(\frac{C_{O_2,ref}}{C_{O_2}} \right)^{0.75} \frac{i}{i_{0,c}^{ref}} \right] \tag{15}$$

Resistance loss and concentration loss occur according to the structural characteristics of the fuel cell (thickness, electronic conductivity, porosity, etc.) and represent losses by hindering the movement of hydrogen protons and electrons. To express η_{ohm} and η_{con} , Jo and his colleague suggest Equations (16) and (17) [37]. Because the resistance of the electron flow (R_{elec}) is small compared to the resistance of the proton flow in Equation (16), it is considered an insignificant term, as in other research [25].

$$\eta_{ohm} = i \left(\frac{\delta_{mem}}{\kappa} + \frac{0.5\delta_{aCL}}{v_{aCL}^{1.5}\kappa} + \frac{0.5\delta_{cCL}}{v_{cCL}^{1.5}\kappa} + R_{elec} \right) \tag{16}$$

$$\eta_{con} = \frac{RT}{4F} \ln \left(\frac{v_{GDL}^{1.5} D_{O_2} C_{O_2}}{v_{GDL}^{1.5} D_{O_2} C_{O_2} - \delta_{GDL}} \right) \tag{17}$$

The parameters in Equations (14)–(17) are shown in Table 3.

The current density of a stack (i) is a function of the H₂ molar flow rate (n_{H_2}) entering the stack, the fuel utilization efficiency (U_f), the MEA area (A_{MEA}), and the number of cells (n_{cell}), as shown in Equation (18).

$$i = n_{H_2} \times U_f \times \frac{2F}{A_{MEA} n_{cell}} \tag{18}$$

The fuel utilization efficiency is shown by Equation (19) and is defined by the ratio of the fuel used by the HT-PEMFC to generate power to the total fuel supplied to the HT-PEMFC [35].

$$U_f = \frac{\text{amount of } H_2 \text{ actually used in the power generation}}{\text{Amount of } H_2 \text{ actually supplied to the stack}} \quad (19)$$

The total energy efficiency of the whole system is defined as the ratio between the produced energy and the supplied energy and can be calculated by Equation (20) [40,41]

$$\eta_{SYS} = \frac{P_{stack}}{(n_{BNG} + n_{PNG}) * LHV_{NG}} \quad (20)$$

In Equation (20), P_{stack} is the power (J/s), n_{BNG} is the number of moles of natural gas supplied to the burner (mol/s), n_{PNG} is the number of moles of natural gas supplied to the reformer (mol/s), and LHV_{NG} is the lower heating value of the natural gas (J/mol).

Table 3. PEMFC parameters used in the combined fuel processor and PEMFC simulation.

Symbol	Value	Unit	Description	Reference
A_{MEA}	300	cm ²	MEA area	-
F	96,500	C/mol	Faraday constant	-
n_{cell}	160	EA	Number of cells	-
R	8.314	J/mol K	Universal gas constant	-
T_{cell}	150	°C	Temperature of cells	-
δ_{aCL}	0.015	mm	Thickness of anode/cathode GDLs, CLs	[37]
δ_{cCL}	0.015	mm	Thickness of anode/cathode GDLs, CLs	[37]
δ_{mem}	0.35	mm	Thickness of anode/cathode GDLs, CLs	[37]
κ	300	S/m	Electronic conductivity	[37]
$i_{0,a}^{ref}$	10 ⁹	A/m ²	Reference exchange current density in anode	[36]
$i_{0,c}^{ref}$	10 ⁴	A/m ²	Reference exchange current density in cathode	[36]
α_a	0.5		Anode transfer coefficient	[38]
α_c	0.65		Cathode transfer coefficient	[38]
$C_{H_2,ref}$	40.88	mol/m ³	Reference H ₂ molar concentration	[38]
$C_{O_2,ref}$	40.88	mol/m ³	Reference O ₂ molar concentration	[38]
v_{aCL}	0.4		Porosity of CL	[38]
v_{cCL}	0.4		Porosity of CL	[38]
v_{GDL}	0.6		Porosity of CL	[38]

3. Result

3.1. Sensitivity Analysis

The simulation results (Figure 6) show the mole fraction of the gas produced in the steam reformer at 500~900 °C. As the temperature of the steam reformer increases, the mole concentration of hydrogen increases, and the thermal efficiency of the fuel processor increases, and they are stabilized at 700 °C or higher. The highest thermal efficiency of the fuel processor is confirmed to be 89.15% at 900 °C, 88.38% at 800 °C, and 86.36% at 700 °C. In order to prevent the degradation of the catalysts, the operating temperature should be lower than 800 °C [42].

Figures 7 and 8 are the simulation results of the mole fraction and thermal efficiency of the fuel processor according to the HTS and LTS temperatures. For the HTS, the thermal efficiency of the fuel processor was 86.36%, regardless of temperature. For the LTS, the thermal efficiency of the fuel processor was decreased by 2% when the temperature was increased from 200 °C (86.36%) to 300 °C (84.36%). Since the HTS and LTS generate a relatively smaller amount of hydrogen compared to the steam reformer, the contribution to the thermal efficiency of the fuel processor according to the temperature change of the HTS or LTS is not significant. Therefore, the operating temperature of the HTS was fixed at

400 °C [26], and the operating temperature of the LTS was fixed at 200 °C in the simulation so that the HTS and LTS each showed the highest efficiency.

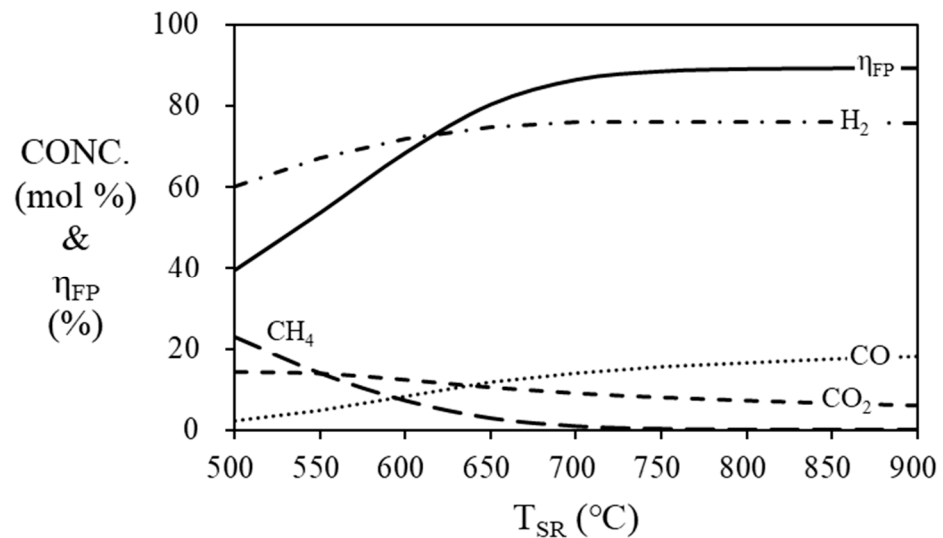


Figure 6. Mole fraction at the outlet of the steam reformer and the efficiency of the fuel processor according to the temperature of the steam reformer. ($S/C = 3$, $T_{HTS} = 400$ °C, and $T_{LTS} = 200$ °C).

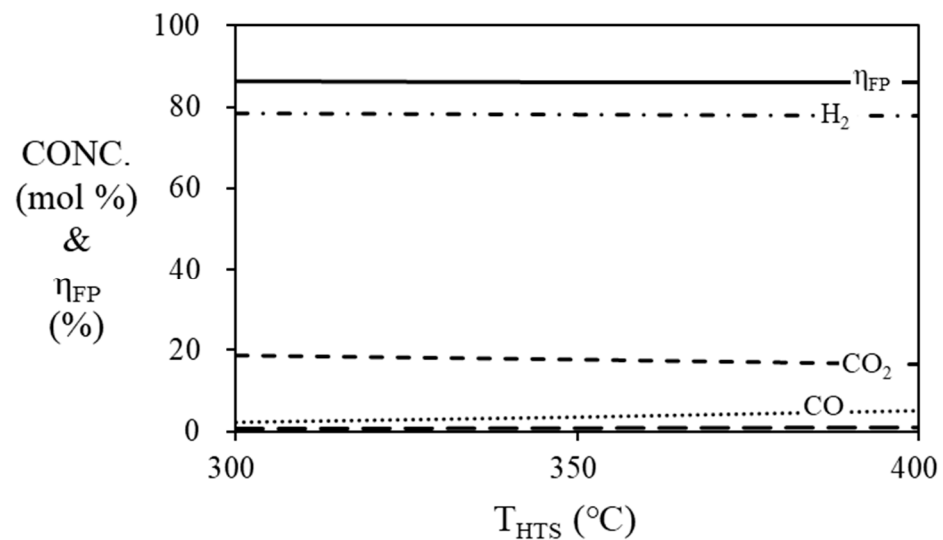


Figure 7. Mole fraction at the outlet of the HTS and efficiency of the fuel processor according to the temperature of the HTS. ($S/C = 3$, $T_{SR} = 700$ °C, and $T_{LTS} = 200$ °C).

The dependence of the CO tolerance of the HT-PEMFC was experimentally confirmed by Das and co-workers, who found that the CO tolerance of the HT-PEMFC increased with increasing temperature. According to their study, the CO tolerance of the HT-PEMFC increased by up to 5% of CO at 180 °C [43]. They also found that no degradation in performance was observed below 0.6 A/cm² at 180 °C as the CO concentration increased from 2% to 5%. On the other hand, at 140 °C and 160 °C, the performance degradation was 17.5% and 12.5%, respectively. This CO tolerance enables options for different CO removal processes in fuel processing systems. The CO generated at the HTS and LTS in Figures 7 and 8 are 5.03% and 0.46%, respectively. Based on this result, a single water–gas shift reactor may be sufficient to supply H₂ to the HT-PEMFC. However, this topic will not be discussed in this study as additional analysis is required to re-engineer the process.

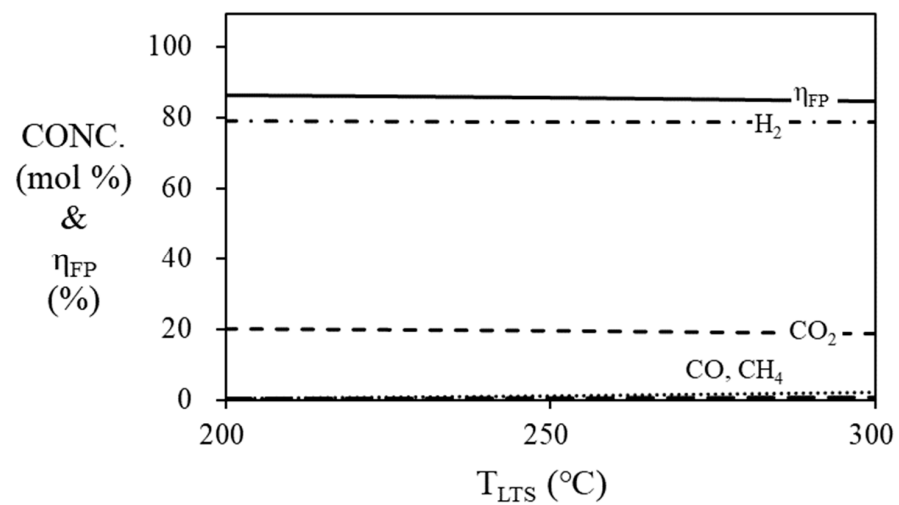


Figure 8. Mole fraction at the outlet of the LTS and efficiency of the fuel processor according to the temperature of the LTS. ($S/C = 3$, $T_{SR} = 700$ °C, and $T_{HTS} = 400$ °C).

As shown in Figure 9 and Table 4, the thermal efficiency of the fuel processor increases as the S/C ratio increases at steam reformer temperatures below 650 °C. As the steam reformer temperature increases, the thermal efficiency of the fuel processor increases. However, the thermal efficiency according to the S/C ratio seems to have a maximum point, according to the S/C ratio, at a temperature of 650 °C or higher in the steam reformer. At a steam reformer temperature of 650 °C, the highest efficiency was 81.81% at an S/C ratio of 4, but at a temperature of 700 °C or higher, the highest efficiency was obtained at an S/C ratio of 3. At a reformer temperature of 700 °C or lower, the highest thermal efficiency of 86.36% was obtained at an S/C ratio of 3.

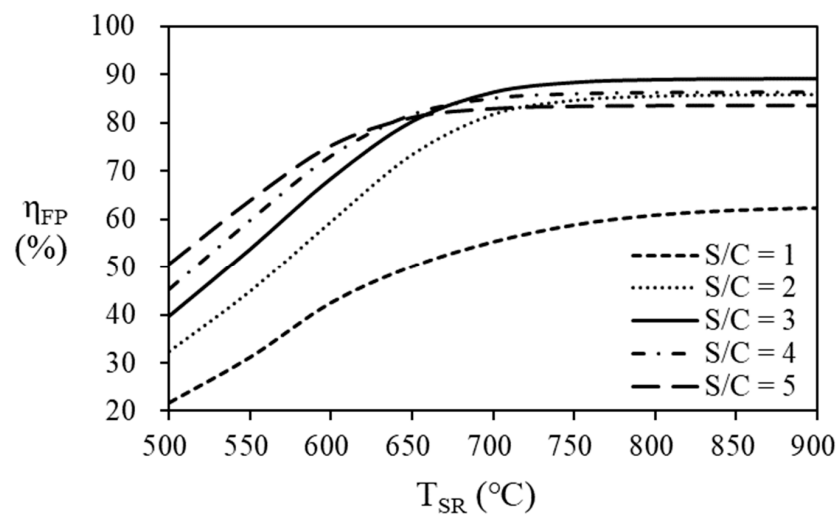


Figure 9. Comparison of the efficiency of the fuel processor according to the temperature of the steam reformer and S/C ratio.

At higher temperatures, the conversion of natural gas to hydrogen increases and more natural gas enters the burner to provide heat to the reactants (natural gas and water) to produce the maximum thermal efficiency at different S/C ratios (and temperatures). Figure 10 shows the conversion of natural gas according to the S/C ratio and temperature of the steam reformer. The conversion of natural gas to hydrogen is calculated based on the molar flow rate of natural gas entering and leaving the steam reformer and indicates the degree of reaction. The amount of heat required to bring the water temperature to the operating temperature of the steam reformer at various S/C ratios and temperatures is

shown in Figure 11. Since a larger amount of water is supplied to the system at a high S/C ratio, the amount of heat required is increased according to the increase in the S/C ratio. On the other hand, since the natural gas conversion is more than 95% at 700 °C and an S/C ratio of 3, the increase in the hydrogen flow rate produced by increasing the S/C ratio at a temperature of 700 °C and higher is inevitably small.

Table 4. Thermal efficiency of the fuel processor corresponding to the steam reformer temperature and S/C ratio. (The bold and border represent the maximum efficiency at the same temperature.)

S/C Ratio \ T _{SR} (°C)		T _{SR} (°C)					
		500	600	650	700	800	900
S/C Ratio	1	21.88	42.64	50.19	55.37	60.93	62.38
	2	32.32	59.54	73.50	81.85	85.60	85.93
	3	39.78	68.52	80.31	86.36	88.94	89.15
	4	45.39	73.25	81.81	85.14	86.32	86.41
	5	50.58	75.31	81.12	82.95	83.56	83.61

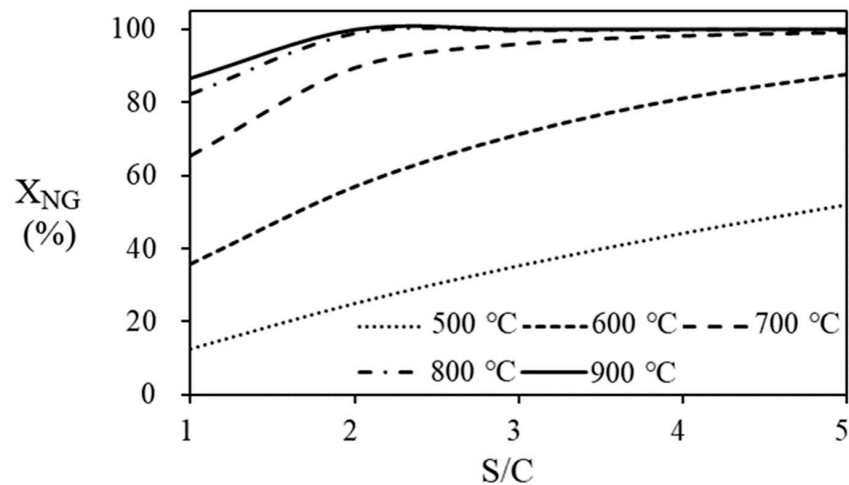


Figure 10. Conversion of natural gas according to the temperature of the steam reformer and S/C ratio.

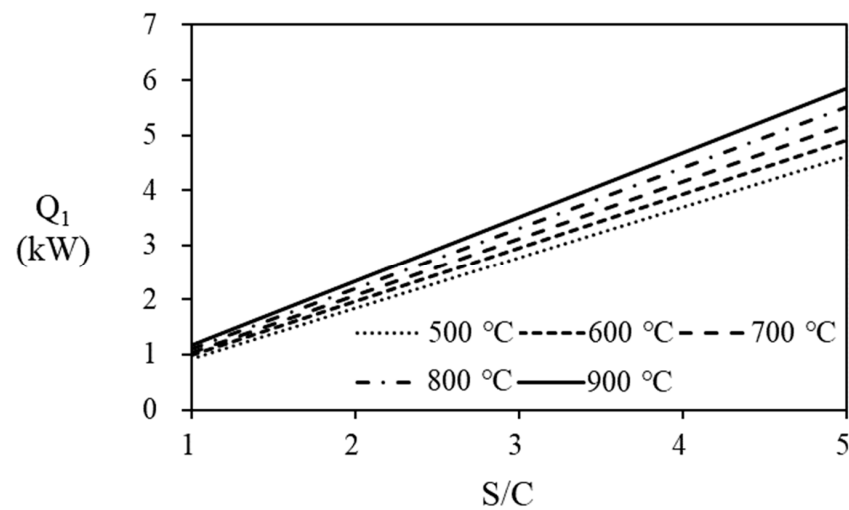


Figure 11. The energy required to heat water according to the S/C ratio and temperature of the steam reformer.

3.2. Anode Off-Gas Recycling

Unreacted hydrogen in the anode off-gas from the PEMFC stack can be recycled as fuel for the steam reformer’s burner, increasing the thermal efficiency of the fuel processor and PEMFC. The thermal efficiency of the combined system depends on the amount of hydrogen recycled, which is determined according to the fuel utilization ratio of the PEMFC. The calculated stack power is summarized in Table 5 and depends on the natural gas supplied to the fuel processor and the fuel utilization efficiency of the stack. In Table 4, the conditions for making more than 5 kW power are shaded. The power increases with a higher fuel utilization at the stack, with higher steam reformer operating temperatures, and with a higher flow rate of PNG. To increase the thermal efficiency of the fuel processor and PEMFC stack, anode off-gas is recycled to the burner. In Figure 12, it can be seen that recycling AOG increases the efficiency of the fuel cell system by 1.28 times compared to the case without it.

Table 5. Power of the fuel cell versus temperature, fuel utilization efficiency, and the molar flow rate of the natural gas process (bold and the border indicates an area that satisfies the target capacity of 5 kW, simulation condition: S/C = 3).

U_f (%)	T_{SR} (°C)	70%			75%			80%		
n_{PNG} (mol/min)		0.7	0.8	0.9	0.7	0.8	0.9	0.7	0.8	0.9
P_{stack} (kW)	600	3.18	3.68	4.18	3.43	3.97	4.51	3.68	4.26	4.84
	650	3.87	4.48	5.09	4.18	4.83	5.48	4.48	5.18	5.88
	700	4.25	4.91	5.58	4.58	5.29	6.01	4.91	5.67	6.44
	750	4.37	5.05	5.74	4.71	5.45	6.19	5.05	5.84	6.63
	800	4.41	5.09	5.79	4.75	5.49	6.24	5.09	5.89	6.69

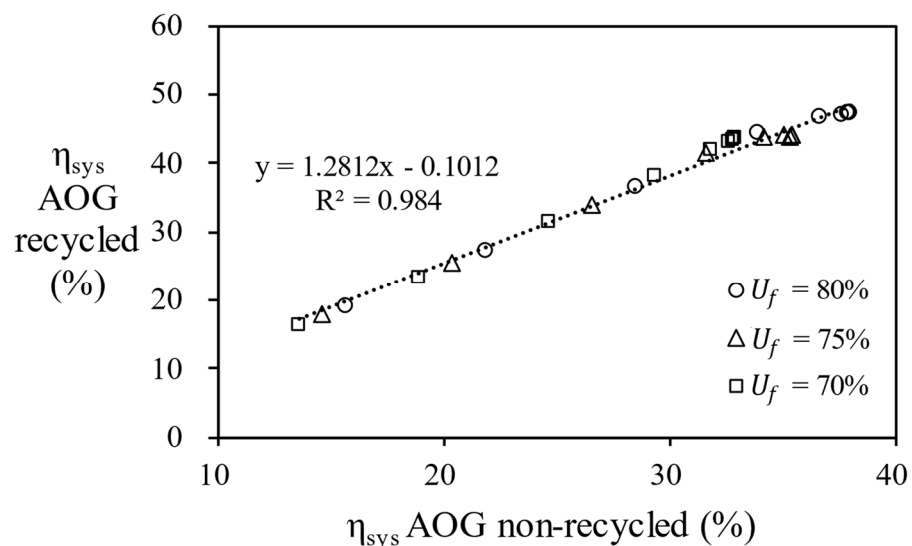


Figure 12. Relationship between the overall system efficiency of the AOG recycling process and the AOG non-recycling process (S/C = 3, n_{PNG} = 0.9 mol/min).

However, some of the calculations are excluded by the details described below in Figure 13. Figure 13 shows the combustion energy generated by each process at various temperatures of the steam reformer. The flow rate of unreacted hydrogen in the anode off-gas varies depending on the fuel utilization (U_f) in the stack, which causes the combustion energy to vary. If the combustion energy of the anode off-gas is greater (red area in Figure 13) than the combustion energy of the natural gas, excess energy is supplied to the reactor, and the reactor temperature increases. Since the use of AOG in this section does

not maintain the temperature, it is excluded from the result of a fuel utilization of 70% or less in this study. Conversely, if the combustion energy of the anode off-gas is smaller (blue area in Figure 13) than the required heat, additional natural gas to the burner must be introduced to maintain the temperature of the reactor.

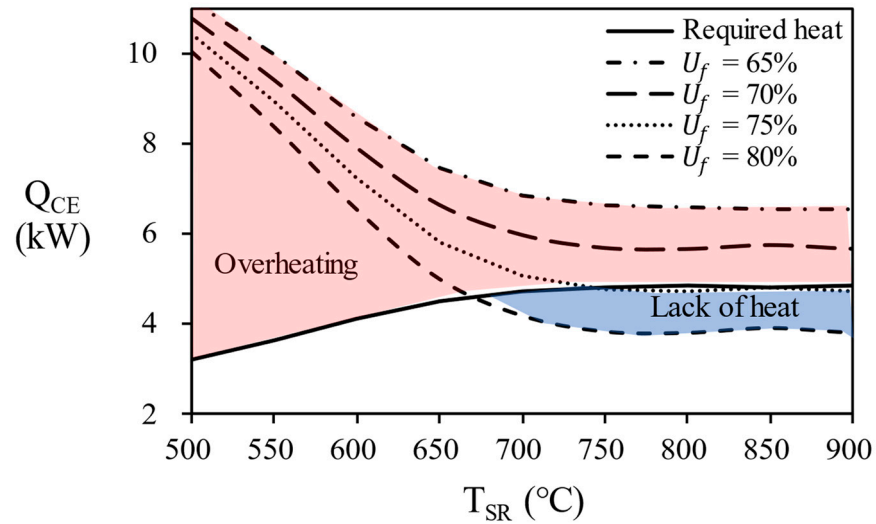


Figure 13. Combustion energy according to the temperature of the steam reformer and the fuel utilization efficiency.

In Figure 14, the overall efficiency of the system is compared according to the temperature of the steam reformer for each process. Since 80% of the AOG has small combustion energy, it is possible to reach maximum efficiency by supplying additional natural gas. Finally, in the case of AOG 75%, the value was consistent with the required heat, showing that the reformer can be operated with only AOG and without an additional fuel supply. In other words, energy independence is possible under the conditions of 750 °C or more, a fuel utilization efficiency = 75%, and S/C = 3.

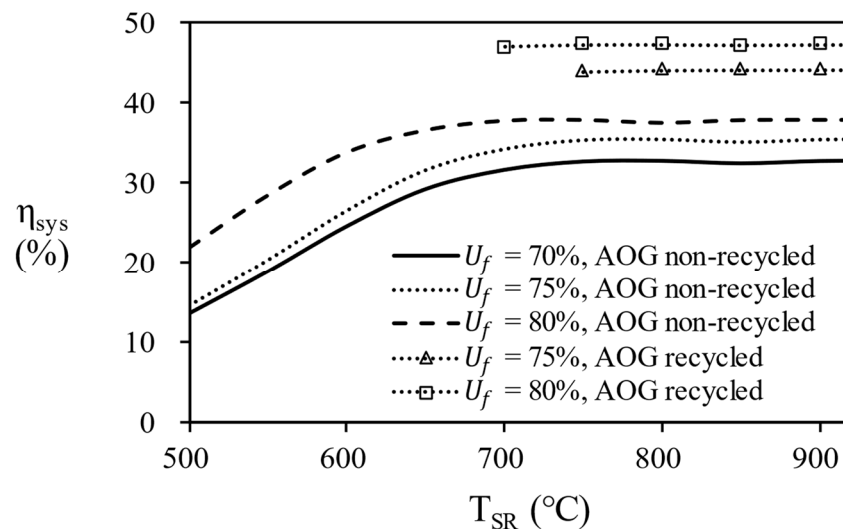


Figure 14. Comparison of system efficiency at various temperatures in AOG recycling and non-recycling operation.

Table 6 shows the final selected operating conditions and system efficiency for a 5 kW residential PEMFC. Consequently, the efficiency of the fuel cell system is recommended under the following conditions: S/C = 3 for maximum efficiency of fuel processor, fuel utilization efficiency without overheating of 75~80%, steam reformer temperature of

700–800 °C, and a molar flow rate of PNG of 0.8–0.9 mol/min to produce more than 5 kW of power.

Table 6. The efficiency of the system for the selected range of temperature, fuel utilization efficiency, and mole flow rate of reactant natural gas.

U_f (%)	T_{SR} (°C)	75%		80%	
n_{PNG} (mol/min)		0.8	0.9	0.8	0.9
η_{sys} (%)	700	43.47	43.79	46.62	46.96
	750	43.74	44.05	46.90	47.24
	800	43.81	44.12	46.98	47.31

4. Conclusions

To increase the overall system efficiency of a combined fuel processor and HT-PEMFC system, the thermal efficiency of the fuel processor must be improved. This study suggests two ways for increasing efficiency:

- (1) Optimize the operating condition (temperature of the reactor, S/C ratio, and reactant flow rate) for high thermal efficiency;
- (2) Recycle the unreacted hydrogen in the anode of HT-PEMFC.

The fuel processor consisting of equilibrium reactors and heat exchangers was analyzed by the Aspen Hysys[®] simulator and the operating conditions were optimized to produce the highest efficiency. In the simulation results, the effect of the temperature change of the WGS was less sensitive than that of the steam reformer, and at maximum efficiency, the operating temperature of the HTS was 400 °C and the operating temperature of the LTS was 200 °C. As the temperature and S/C ratio of the steam reformer increase, the hydrogen concentration of the reformed gas increases, but the thermal efficiency of the fuel processor decreases. The steam reformer showed maximum thermal efficiency at an S/C ratio of 5 at 500 °C, S/C ratio of 4 at 650 °C, and S/C ratio of 3 at 700 °C, 800 °C, and 900 °C. The temperature of the steam reformer was selected to be 700 °C or higher, which is a condition with a methane conversion of 95% or higher. However, the efficiency of the steam reformer at 900 °C was excluded in consideration of catalyst life. The reason for the decrease in efficiency is that the energy required to heat the water is greater than the energy from the produced hydrogen. Recycling unreacted hydrogen as combustion fuel increased the overall efficiency of the combined system by a factor of 1.28. However, excessive heat was supplied to the fuel processor when the fuel utilization efficiency was less than 70% and so this condition was also excluded. As a result, an overall efficiency of 43.47–47.31% was confirmed for the following conditions with a 5 kW power output: $T_{SR} = 700$ °C, 750 °C, and 800 °C, S/C ratio = 3, $n_{PNG} = 0.8$ and 0.9, and $U_f = 75\%$ and 80%. By adding a recycling stream, overall efficiency gains and CO reduction are achieved, reducing the operating costs. Waste heat recovery for HT-PEMFC's tri-generation system could also be another good application to increase overall efficiency. HT-PEMFCs have good CO tolerance and good waste heat quality, allowing for a more economical design of energy production for residential buildings.

Author Contributions: Formal analysis, S.P.; Investigation, S.P.; Writing—original draft, S.P.; Writing—review & editing, S.L.; Supervision, S.L. All authors have read and agreed to the published version of the manuscript.

Funding: This research was funded by Korea Institute of Energy Technology Evaluation and Planning grant number 20183010032400.

Institutional Review Board Statement: Not applicable.

Informed Consent Statement: Not applicable.

Data Availability Statement: Not applicable.

Acknowledgments: The authors are thankful to the Korea Institute of Energy Technology Evaluation and Planning (KETEP) for the support grant funded by the Korean government's Ministry of Trade, Industry, and Energy under the project titled: "Development on localization technologies of export-purposed stationary fuel cell systems", numbered: 20183010032400.

Conflicts of Interest: The authors declare no conflict of interest.

References

1. Nagasawa, K.; Rhodes, J.D.; Webber, M.E. Assessment of Primary Energy Consumption, Carbon Dioxide Emissions, and Peak Electric Load for a Residential Fuel Cell Using Empirical Natural Gas and Electricity Use Profiles. *Energy Build.* **2018**, *178*, 242–253. [[CrossRef](#)]
2. Ozawa, A.; Kudoh, Y. Performance of Residential Fuel-Cell-Combined Heat and Power Systems for Various Household Types in Japan. *Int. J. Hydrogen Energy* **2018**, *43*, 15412–15422. [[CrossRef](#)]
3. Pinto, P.J.R.; Sousa, T.; Fernandes, V.R.; Pinto, A.M.F.R.; Rangel, C.M. Simulation of a Stand-Alone Residential PEMFC Power System with Sodium Borohydride as Hydrogen Source. *Int. J. Electr. Power Energy Syst.* **2013**, *49*, 57–65. [[CrossRef](#)]
4. Yuan, J.; Ren, F.; Sundén, B. Analysis of Chemical-Reaction-Coupled Mass and Heat Transport Phenomena in a Methane Reformer Duct for PEMFCs. *Int. J. Heat Mass Transf.* **2007**, *50*, 687–701. [[CrossRef](#)]
5. Bozorgmehri, S.; Heidary, H.; Salimi, M. Market Diffusion Strategies for the PEM Fuel Cell-Based Micro-CHP Systems in the Residential Sector: Scenario Analysis. *Int. J. Hydrogen Energy* **2023**, *48*, 3287–3298. [[CrossRef](#)]
6. Kim, R.H.; Baek, C.; Kim, E.; Jeong, Y.; Cho, S. Potential Global Warming Impact of 1 KW Polymer Electrolyte Membrane Fuel Cell System for Residential Buildings on Operation Phase. *Energy Sustain. Dev.* **2023**, *73*, 376–386. [[CrossRef](#)]
7. Jo, T.; Koo, B.; Lee, Y.; Kim, D.; Lee, D. Combined Thermal Characteristics Analysis of Steam Reforming and Combustion for 5 KW Domestic PEMFC System. *Int. J. Hydrogen Energy* **2018**, *43*, 14226–14237. [[CrossRef](#)]
8. Pasdag, O.; Kvasnicka, A.; Steffen, M.; Heinzel, A. Highly Integrated Steam Reforming Fuel Processor with Condensing Burner Technology for Maximised Electrical Efficiency of CHP-PEMFC Systems. *Energy Procedia* **2012**, *28*, 57–65. [[CrossRef](#)]
9. Seo, Y.T.; Seo, D.J.; Jeong, J.H.; Yoon, W.L. Design of an Integrated Fuel Processor for Residential PEMFCs Applications. *J. Power Source* **2006**, *160*, 505–509. [[CrossRef](#)]
10. Lee, J.S.; Seo, J.; Kim, H.Y.; Chung, J.T.; Yoon, S.S. Effects of Combustion Parameters on Reforming Performance of a Steam-Methane Reformer. *Fuel* **2013**, *111*, 461–471. [[CrossRef](#)]
11. Seo, Y.-S.; Seo, D.-J.; Seo, Y.-T.; Yoon, W.-L. Investigation of the Characteristics of a Compact Steam Reformer Integrated with a Water-Gas Shift Reactor. *J. Power Source* **2006**, *161*, 1208–1216. [[CrossRef](#)]
12. Jiang, J.; Li, X.; Deng, Z.; Yang, J.; Zhang, Y.; Li, J. Control-Oriented Dynamic Model Optimization of Steam Reformer with an Improved Optimization Algorithm. *Int. J. Hydrogen Energy* **2013**, *38*, 11288–11302. [[CrossRef](#)]
13. Perna, A. Hydrogen from Ethanol: Theoretical Optimization of a PEMFC System Integrated with a Steam Reforming Processor. *Int. J. Hydrogen Energy* **2007**, *32*, 1811–1819. [[CrossRef](#)]
14. Pashchenko, D.; Mustafin, R.; Karpilov, I. Thermochemical Recuperation by Steam Methane Reforming as an Efficient Alternative to Steam Injection in the Gas Turbines. *Energy* **2022**, *258*, 124913. [[CrossRef](#)]
15. Pashchenko, D. Performance Evaluation of a Combined Power Generation System Integrated with Thermochemical Exhaust Heat Recuperation Based on Steam Methane Reforming. *Int. J. Hydrogen Energy* **2023**, *48*, 5823–5835. [[CrossRef](#)]
16. Carapellucci, R.; Giordano, L. Steam, Dry and Autothermal Methane Reforming for Hydrogen Production: A Thermodynamic Equilibrium Analysis. *J. Power Source* **2020**, *469*, 228391. [[CrossRef](#)]
17. Jannelli, E.; Minutillo, M.; Perna, A. Analyzing Microgeneration Systems Based on LT-PEMFC and HT-PEMFC by Energy Balances. *Appl. Energy* **2013**, *108*, 82–91. [[CrossRef](#)]
18. Choi, M.; Kim, M.; Sohn, Y.-J.; Kim, S.-G. Development of Preheating Methodology for a 5 KW HT-PEMFC System. *Int. J. Hydrogen Energy* **2021**, *46*, 36982–36994. [[CrossRef](#)]
19. Suwanmanee, U.; Saebea, D.; Hacker, V.; Assabumrungrat, S.; Arpornwichanop, A.; Authayanun, S. Conceptual Design and Life Cycle Assessment of Decentralized Power Generation by HT-PEMFC System with Sorption Enhanced Water Gas Shift Loop. *Energy Convers. Manag.* **2018**, *171*, 20–30. [[CrossRef](#)]
20. Naseem, M.; Park, S.; Lee, S. Experimental and Theoretical Analysis of a Trigeration System Consisting of Adsorption Chiller and High Temperature PEMFC. *Energy Convers. Manag.* **2022**, *251*, 114977. [[CrossRef](#)]
21. Dalle Nogare, D.; Baggio, P.; Tomasi, C.; Mutri, L.; Canu, P. A Thermodynamic Analysis of Natural Gas Reforming Processes for Fuel Cell Application. *Chem. Eng. Sci.* **2007**, *62*, 5418–5424. [[CrossRef](#)]
22. Kim, D.; Jo, T.; Koo, B.; So, H.; Lee, Y.; Lee, D. Combustion Characteristics of Anode Off-Gas on the Steam Reforming Performance. *Int. J. Hydrogen Energy* **2019**, *44*, 4688–4697. [[CrossRef](#)]
23. Powell, M.; Meinhardt, K.; Sprengle, V.; Chick, L.; McVay, G. Demonstration of a Highly Efficient Solid Oxide Fuel Cell Power System Using Adiabatic Steam Reforming and Anode Gas Recirculation. *J. Power Source* **2012**, *205*, 377–384. [[CrossRef](#)]
24. Lee, K.; Yun, J.; Ahn, K.; Lee, S.; Kang, S.; Yu, S. Operational Characteristics of a Planar Steam Reformer Thermally Coupled with a Catalytic Burner. *Int. J. Hydrogen Energy* **2013**, *38*, 4767–4775. [[CrossRef](#)]

25. Perna, A.; Cicconardi, S.P.; Cozzolino, R. Performance Evaluation of a Fuel Processing System Based on Membrane Reactors Technology Integrated with a PEMFC Stack. *Int. J. Hydrogen Energy* **2011**, *36*, 9906–9915. [[CrossRef](#)]
26. Peters, R.; Deja, R.; Engelbracht, M.; Frank, M.; Nguyen, V.N.; Blum, L.; Stolten, D. Efficiency Analysis of a Hydrogen-Fueled Solid Oxide Fuel Cell System with Anode off-Gas Recirculation. *J. Power Source* **2016**, *328*, 105–113. [[CrossRef](#)]
27. Pasel, J.; Samsun, R.C.; Schmitt, D.; Peters, R.; Stolten, D. Test of a Water–Gas-Shift Reactor on a 3kWe-Scale—Design Points for High- and Low-Temperature Shift Reaction. *J. Power Source* **2005**, *152*, 189–195. [[CrossRef](#)]
28. Dejong, M.; Reinders, A.; Kok, J.; Westendorp, G. Optimizing a Steam-Methane Reformer for Hydrogen Production. *Int. J. Hydrogen Energy* **2009**, *34*, 285–292. [[CrossRef](#)]
29. Salahi, F.; Zarei-Jelyani, F.; Farsi, M.; Rahimpour, M.R. Optimization of Hydrogen Production by Steam Methane Reforming over Y-Promoted Ni/Al₂O₃ Catalyst Using Response Surface Methodology. *J. Energy Inst.* **2023**, *108*, 101208. [[CrossRef](#)]
30. Huang, X.; Lv, Z.; Zhao, B.; Zhang, H.; Yao, X.; Shuai, Y. Optimization of Operating Parameters for Methane Steam Reforming Thermochemical Process Using Response Surface Methodology. *Int. J. Hydrogen Energy* **2022**, *47*, 28313–28321. [[CrossRef](#)]
31. Twigg, M.V. *Catalyst Handbook*, 2nd ed.; Wolfe Publishing Ltd.: London, UK, 1989; Butler & Tanner; ISBN 0-7234-0857-2.
32. Feitelberg, A.S.; Rohr, D.F. Operating Line Analysis of Fuel Processors for PEM Fuel Cell Systems. *Int. J. Hydrogen Energy* **2005**, *30*, 1251–1257. [[CrossRef](#)]
33. Hagh, B.F. Stoichiometric Analysis of Autothermal Fuel Processing. *J. Power Source* **2004**, *130*, 85–94. [[CrossRef](#)]
34. Lutz, A.; Bradshaw, R.; Keller, J.; Witmer, D. Thermodynamic Analysis of Hydrogen Production by Steam Reforming. *Int. J. Hydrogen Energy* **2003**, *28*, 159–167. [[CrossRef](#)]
35. O’Hayre, R.; Cha, S.-W.; Colella, W.; Prinz, F.B. *Fuel Cell Fundamentals*, 3rd ed.; John Wiley & Sons, Inc.: Hoboken, NJ, USA, 2016; ISBN 978-1-119-19176-6.
36. Chippar, P.; Ju, H. Three-Dimensional Non-Isothermal Modeling of a Phosphoric Acid-Doped Polybenzimidazole (PBI) Membrane Fuel Cell. *Solid State Ion.* **2012**, *225*, 30–39. [[CrossRef](#)]
37. Jo, A.; Oh, K.; Lee, J.; Han, D.; Kim, D.; Kim, J.; Kim, B.; Kim, J.; Park, D.; Kim, M.; et al. Modeling and Analysis of a 5 KW_e HT-PEMFC System for Residential Heat and Power Generation. *Int. J. Hydrogen Energy* **2017**, *42*, 1698–1714. [[CrossRef](#)]
38. Won, S.; Oh, K.; Ju, H. Numerical Degradation Studies of High-Temperature Proton Exchange Membrane Fuel Cells with Phosphoric Acid-Doped PBI Membranes. *Int. J. Hydrogen Energy* **2016**, *41*, 8296–8306. [[CrossRef](#)]
39. Jiao, K.; Li, X. A Three-Dimensional Non-Isothermal Model of High Temperature Proton Exchange Membrane Fuel Cells with Phosphoric Acid Doped Polybenzimidazole Membranes. *Fuel Cells* **2010**, *10*, 351–362. [[CrossRef](#)]
40. Arsalis, A.; Nielsen, M.P.; Kær, S.K. Modeling and Optimization of a 1 KW_e HT-PEMFC-Based Micro-CHP Residential System. *Int. J. Hydrogen Energy* **2012**, *37*, 2470–2481. [[CrossRef](#)]
41. Godat, J.; Marechal, F. Optimization of a Fuel Cell System Using Process Integration Techniques. *J. Power Source* **2003**, *118*, 411–423. [[CrossRef](#)]
42. Carrasco-Ruiz, S.; Zhang, Q.; Gándara-Loe, J.; Pastor-Pérez, L.; Odriozola, J.A.; Reina, T.R.; Bobadilla, L.F. H₂-Rich Syngas Production from Biogas Reforming: Overcoming Coking and Sintering Using Bimetallic Ni-Based Catalysts. *Int. J. Hydrogen Energy* **2023**, *48*, S0360319923014246. [[CrossRef](#)]
43. Das, S.K.; Reis, A.; Berry, K.J. Experimental Evaluation of CO Poisoning on the Performance of a High Temperature Proton Exchange Membrane Fuel Cell. *J. Power Source* **2009**, *193*, 691–698. [[CrossRef](#)]

Disclaimer/Publisher’s Note: The statements, opinions and data contained in all publications are solely those of the individual author(s) and contributor(s) and not of MDPI and/or the editor(s). MDPI and/or the editor(s) disclaim responsibility for any injury to people or property resulting from any ideas, methods, instructions or products referred to in the content.